ELSEVIER

Contents lists available at ScienceDirect

## Composites Part B

journal homepage: www.elsevier.com/locate/compositesb





# Enhanced energy mitigation of thin-walled tube filled with liquid nanofoam under dynamic impact

Mingzhe Li<sup>a</sup>, Saeed Barbat<sup>b</sup>, Ridha Baccouche<sup>b</sup>, Jamel Belwafa<sup>b</sup>, Weiyi Lu<sup>a,\*</sup>

- <sup>a</sup> Department of Civil and Environmental Engineering, Michigan State University, East Lansing, MI, 48824, USA
- <sup>b</sup> Ford Motor Company, Dearborn, MI, 48121, USA

#### ARTICLE INFO

Keywords:
Foam-filled tube
Liquid nanofoam
Interfacial bonding
Filler-tube wall interaction
Energy absorption
Vehicle crashworthiness

#### ABSTRACT

Due to the intimate contact between the fluid-like liquid nanofoam (LN) filler and the tube wall, the filler-tube wall interaction in LN-filled tube (LNFT) is enhanced, leading to a much-improved performance of the composite structure. However, a comprehensive understanding of the energy mitigation performance and the underlying working mechanism of LNFT is still lacking. This study aims to explore the crushing behavior of LNFT subjected to quasi-static compression and dynamic impact and reveal the working mechanism of LNFT at different strain rates and the selection criteria for LN filler and tube wall material. A series of quasi-static compression tests are conducted on LNFTs with various LN fillers. The strengthening coefficient of LNFT is larger than 3.5. Micro-CT images show that the LN-tube interaction improves the performance of LNFT through extended plastic deformation of the tube wall. Under dynamic impacts, the energy absorption capacity of LNFT shows 54% increase compared to that under quasi-static tests, leading to a remarkable strengthening coefficient of 8.0. The strain rate effect is due to the different energy mitigation mechanisms of the LN-filler, i.e. energy dissipation at lower strain rate and energy capture at higher strain rate. To optimize the impact mitigation performance of LNFT, the most critical system parameters are the infiltration pressure and total pore volume of the LN-filler and the stiffness and ductility of the tube wall. These findings and research outcomes expedite the understanding of the impact mitigation mechanism of LNFT and provide design guidance for the LN-based composite structures.

## 1. Introduction

Over the past decades, enormous efforts have been made to develop energy mitigation materials and structures for prevention of personnel injuries or key facilities damages [1]. Among many others, thin-walled metallic tubes have been widely used as energy mitigating devices due to their light weight, low cost, and easiness to manufacture [2,3]. The axial plastic buckling of tube wall is known as the main energy mitigation mechanism of thin-walled tubes. However, the sudden drop from the initial buckling strength to the post-buckling strength dramatically reduces the energy mitigation efficiency of the thin-walled tubes. The foam filling method, which creates a shell-core composite structure, has been utilized to enhance the post-buckling strength and deformation stability of thin-walled tubes [4,5]. Metallic foams [6–10] and polymeric foams [11,12] are commonly used filling materials. To further improve the performance of foam-filled tubes, various strategies have also been developed, including but not limited to metallic syntactic foams [13–16], graded foam filler [17–20], topology optimization [21],

bitubal structures [22,23], tube-reinforced foam [24], metal/CFRP hybrid structures [25], GFRP tubes [26], periodic cellular structures [27], multiscale bio-structures [28]. As regards the reinforcing mechanism, it has been found that the overall crush response of foam-filled tubes comprises the yielding of tube, the collapse of foam and the filler-tube wall interaction [22,29]. Santosa et al. [30] have used combined experimental and numerical approach to find that the strengthening coefficient of Al foam filler is 1.8, i.e. the contribution from filler-tube wall interaction accounts for 80% of the foam strength. The filler-tube wall interaction has been further attributed to the strain hardening of the tube wall as well as the load transfer effect between filler and tube wall.

To further improve the crush resistance of the shell-core composite structure, it is critical to strengthen the interfacial bonding between the filler and tube wall. By adding adhesive at the interface, the foam strengthening coefficient has increased from 1.8 to 2.8 [30–32]. However, the multistep adhesion process is not cost-effective and time-consuming [32–34]. Direct *in situ* foaming inside the hollow tube

E-mail address: wylu@egr.msu.edu (W. Lu).

<sup>\*</sup> Corresponding author.

has been proposed to facilitate the bonding formation at the interface. Although the resulted composite tubes have shown enhanced energy mitigation performance, the foaming process is difficult to control [35], and the synthesized foam filler is susceptible to process-induced structural defects such as foam shrinkage, metal drainage and pore coalescence [31,36]. More importantly, the interfacial bonding generated by these methods inevitably contains imperfections. As the tube wall buckling progresses, debonding initiates from these imperfections. Consequently, the filler-tube wall interaction is weakened or even diminished. The loss of the filler-tube wall interaction leads to a much reduced energy mitigation performance [30], which demonstrates that the filler-tube interaction is more efficient than debonding or friction in foam-filled tubes for energy mitigation [37,38].

Employing liquid filler in thin-walled structures is another promising approach to create seamless interface between filler and tube wall. Compared with solid foam fillers, liquids can maintain intimate contact with the tube wall at any degree of deformation, due to the intrinsic fluidity. The resulted "perfect interfacial bonding" maximizes the filler-tube wall interaction and significantly enhances the crushing performance of the solid shell-liquid core structure. However, conventional liquids are nearly incompressible, and the total deformability of the structure is severely compromised. In this regard, a highly compressible liquid filler is essential to achieve the seamless interface without sacrificing the total deformability of the shell-core composite structure.

To address the above concerns, a nanofluidics-based energy mitigation material with high compressibility, namely liquid nanofoam (LN), has been developed [39–41]. LN composes of nanoporous particles and a non-wettable liquid. The nanopore surface is surface treated and hydrophobic. When the nanoporous particles are immersed into a liquid phase, the liquid molecules stay outside of the nanopores at ambient condition due to the capillary effect. As a sufficient external pressure is applied, the surface resistance is overcome and the liquid molecules are driven into the nanopores. The resulted highly hysteretic loading-unloading process suggests that tremendous amount of energy is mitigated [42]. Besides, it has been experimentally demonstrated that the LN system has high structural integrity [43], ultra-fast response to external impact [44], and a novel energy mitigation mechanism at increased strain rates [45–47], making it a promising filler candidate in thin-walled tubes for applications under high strain rates.

Recently, LN-filled tube (LNFT) has drawn increasing attention from automotive industry for potential applications including crash box and accelerator pedal [48]. Several studies have been conducted to evaluate both quasi-static [49,50] and dynamic [51,52] behaviors of LNFT. Li et al. [52] have studied the underpinning energy mitigation mechanism of the LNFT and revealed that the filler-tube wall interaction is the dominating working mechanism. Due to the "perfect liquid-solid bonding" at the LN-tube wall interface, the filler-tube wall interaction is much enhanced, as indicated by a strengthening coefficient of 3.8. For real case scenarios such as automobile collision and blasts, external impacts with extremely high energy and incident speed will be exerted on the energy mitigation materials. In addition, practical applications require larger scale LNFTs than the smaller scale ones studied in literature. So far, the effect of LN filler and the tube wall material on the overall performance of the LN-based composite structure remains unclear. Design criteria of the LNFT are still lacking. To this end, large scale LNFTs have been prepared and the crushing behavior has been evaluated in this study. The effects of LN, tube wall material and strain rate on the energy mitigation performance and filler-tube wall interaction of LNFT have been investigated. The enhanced plastic deformation of tube wall caused by filler-tube wall interaction has also been visualized.

## 2. Material and methods

## 2.1. Materials and sample preparation

The thin-walled tube used in this study was made of Al 6061 and

obtained from McMaster (Product No. 9056k85). The outer diameter, wall thickness and height of the Al tube were  $D=76.2\,mm$ ,  $t=1.63\,mm$  and  $h_0=101.6\,mm$ , respectively. The Al tube was filled with LN and then sealed by clamping both ends to two stainless steel caps equipped with nitrile rubber O-rings. The effective height of the tube was  $h=81.3\,mm$ , as shown in Fig. 1a. Empty Al tube was used as reference. During all experiments, no liquid leakage was observed at the sealing sections. Fig. 1 shows details of a typical LNFT sample.

The LN fillers used in this study contained a same nanoporous silica gel (denoted as SG90) purchased from Sigma-Aldrich (Product No. 60759) and various aqueous solutions. The average nanopore size and particle size of SG90 were 7.8 nm and 40–63  $\mu m$  [53], respectively. As illustrated in Fig. 2, SG90 particles were irregular and the porous structure was open. The as received SG90 had chloro(dimethyl)octylsilane modified surface, which was non-wettable to the aqueous solution. The porous structure as well as the surface condition of these nanoporous particles dominated the mechanical response of the LN.

#### 2.2. Test procedures

The crush response of empty tubes and LNFTs were characterized by a series of quasi-static compression tests and gas gun impact tests. The quasi-static compression tests were conducted by using a hydraulic driven MTS system (300 kN load capacity) at a constant loading speed of 2 mm/s. Fig. 3a shows the experimental setup of quasi-static compression test. The nominal stress was calculated as  $\sigma=F/A$ , where F was the force applied by the MTS machine and A was the cross-sectional area of Al tubes. The nominal strain was calculated as  $\varepsilon=\delta/h$ , where  $\delta$  was the crosshead displacement of the MTS machine.

The dynamic behavior of the Al tubes was characterized by a customized gas gun apparatus at Ford Motor Company, as shown in Fig. 3b. The carriage weight was 181.55 kg. The incident speed was maintained at 6.7 m/s by controlling the pressure of the gas reservoir. The load-time history F(t) of the tube samples was measured by two load sensors (500 kN load capacity). One fixed on the stopper and the other on the carriage front. The nearly identical load-time histories measured by both load sensors confirmed that the LNFT samples deformed under stress equilibrium condition under dynamic impacts. An accelerometer was attached to the carriage to measure its deceleration time-history, a(t). The deformation process of the tubes under gas gun impact was recorded by high speed cameras. The incident speed was determined by  $v=\int a(\tau)d\tau$ . The displacement was calculated as  $\delta=\int\!\!\! f a(\tau)d^2\tau$ .

## 3. Results and discussion

## 3.1. Compressive behavior of empty Al tubes

Typical stress-strain curves under both quasi-static compression and gas gun impact are shown in Fig. 4. Under quasi-static compression, the empty Al tube wall buckling initiation occurs at 23 MPa after a sharp elastic response in the beginning. As the buckling progresses, the stress drops quickly and forms a low post-buckling plateau. The jerky stress plateau reflects the fold initiation, formation and collapse. The mean post-buckling stress is 9.8 MPa. Fig. 4b shows that the empty tube deforms in a diamond mode and has a concertina lobe at the top, which is due to the initial axisymmetric trigger [54]. As the buckling is triggered, non-axisymmetric folds with 3 corners per lobe form sequentially along the tube length. This buckling mode of empty Al tubes is consistent with literature results [32,52,54,55].

As the dynamic impact is applied, a low post-buckling stress plateau forms after buckling initiation (Fig. 4a), similar to that in quasi-static compression test. The first peak around 4 MPa is due to the subtle misalignment of the top and bottom of the empty tubes, which is created during the tube cutting process. The lower buckling initiation stress is due to the instability-induced buckling mode change under dynamic

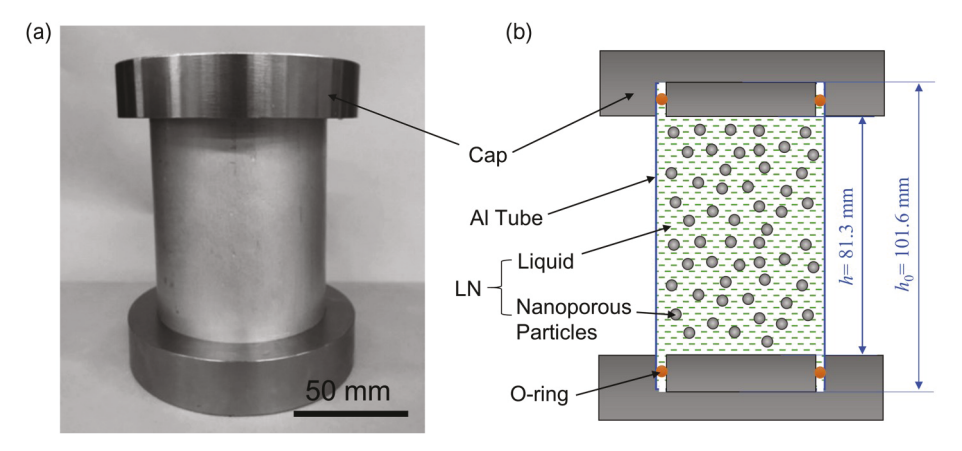


Fig. 1. (a) A typical LNFT sample (b) Cut view of the LNFT.

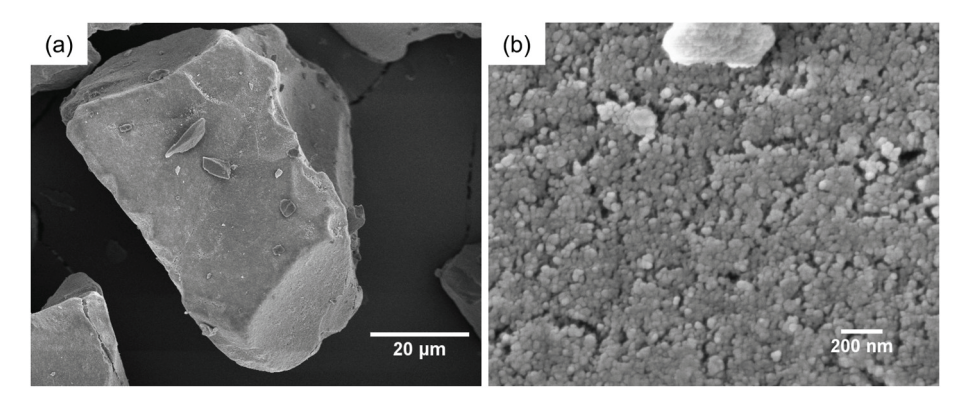


Fig. 2. SEM images of the nanoporous particles (a) a single SG90 nanoporous particle (b) nanoporous structure of SG90.

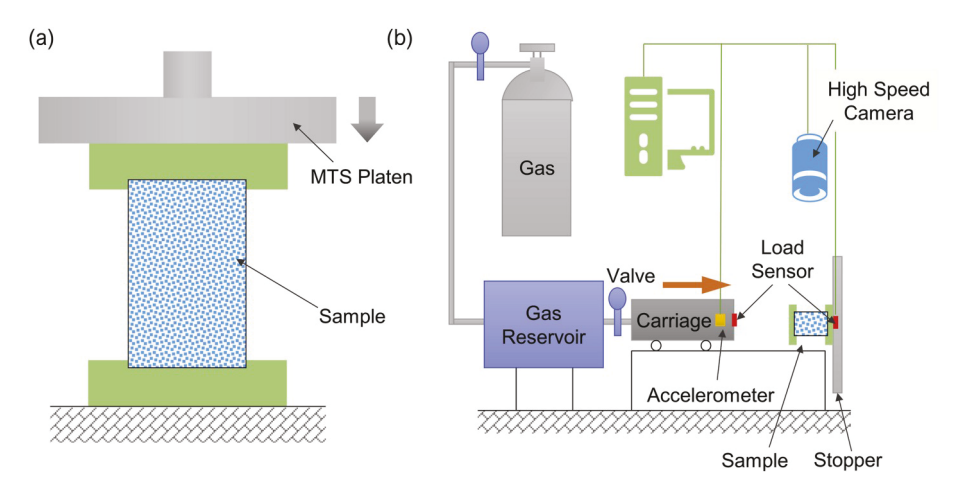


Fig. 3. (a) Schematic of the quasi-static compression test with loading speed of 2 mm/s (b) Schematic of the gas gun apparatus for dynamic impacts at incident speed of 6.7 m/s.

impact (Fig. 4b and c). Fig. 4c shows the snapshots of empty Al tube under gas gun impact. The empty tube buckles inwards in a diamond mode with 3 corners per lobe, same as that in quasi-static compression test. However, the concertina lobe at the top cannot be observed in the dynamic test. This is attributed to the instability under dynamic impact, leading to a non-axisymmetric trigger at the beginning. The mean post-buckling stress of empty tubes in gas gun impact test is 10.8 MPa, 10% higher than that in quasi-static compression test. This is due to the strain rate sensitivity of the Al material [56].

## 3.2. Compressive behavior of LNs

Three different LN systems (denoted as LN-1, LN-2, and LN-3) are selected as the filling material in current study. The nanoporous material in these three LNs is SG90. The liquid phases in the LNs are DI water, 10 wt% ethanol aqueous solution and 15 wt% ethanol aqueous solution, respectively. Fig. 5 shows typical mechanical behavior of the LNs. In our previous result [52], it has been demonstrated that the mechanical behavior of the LNs is strain rate independent. As LN-1 is compressed, initially, the LN system shows an elastic behavior and the volume

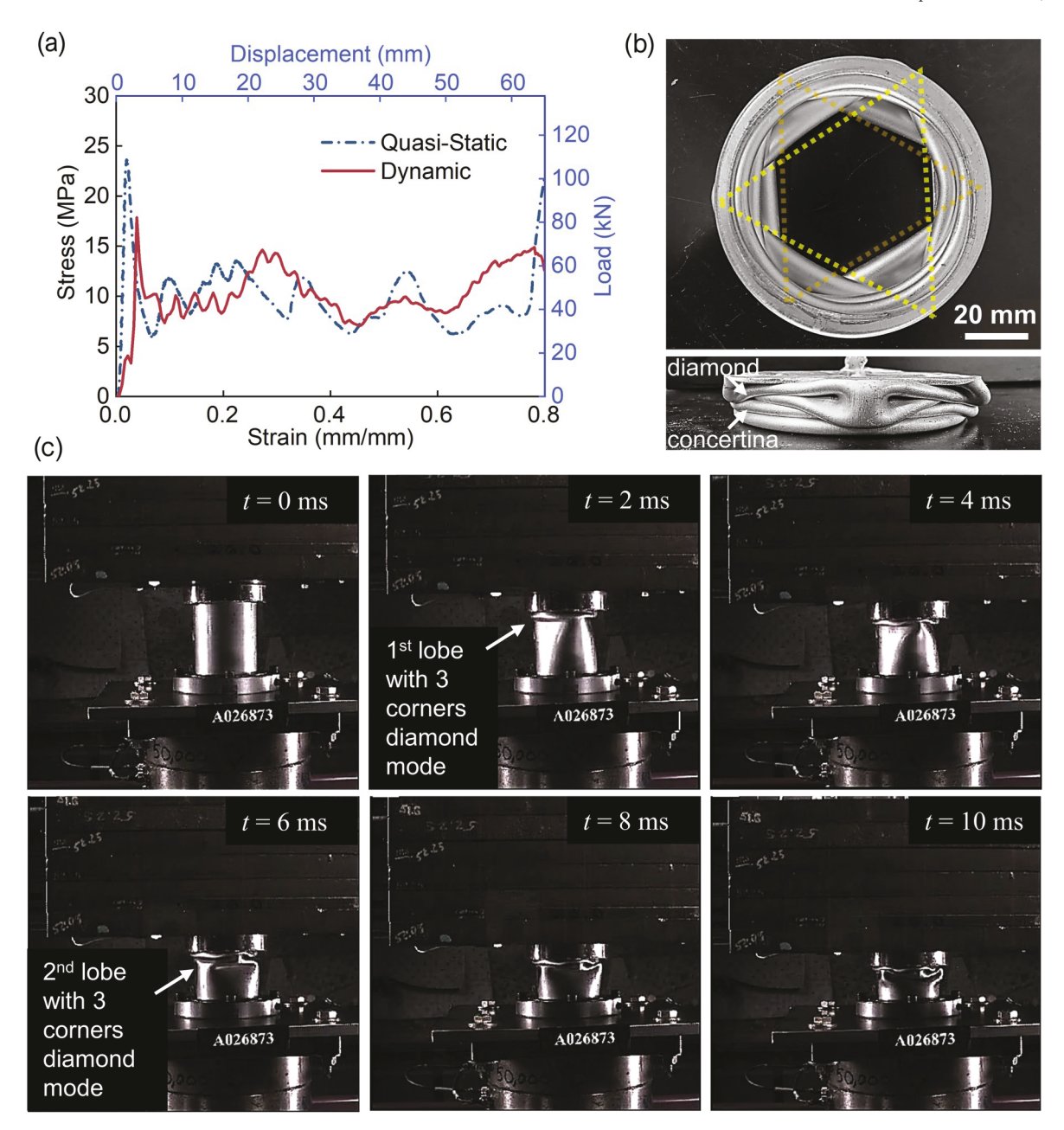


Fig. 4. (a) Typical stress-strain curves of empty Al tubes under quasi-static compression and gas gun impact. Stress-strain and load-displacement axes are interchangeable. (b) Snapshots of the deformation mode of empty Al tubes under quasi-static compression. The yellow triangle denotes the shape of one lobe (c) Snapshots of the deformation mode of empty Al tubes under gas gun impact. (For interpretation of the references to color in this figure legend, the reader is referred to the Web version of this article.)

change is relatively small. As the pressure reaches an initial pressure,  $P_{\rm i}=15$  MPa, the system becomes highly compressible and a wide stress plateau is observed. This indicates that the capillary effect of the hydrophobic nanopores is overcome and the water molecules are forced into the nanopores. The stress plateau ends at a pressure,  $P_{\rm f}=35$  MPa, at which all nanopores are filled with water molecules and the system becomes incompressible. Thus, the working pressure  $P_{\rm in}$  of LN-1 ranges from 15 to 35 MPa. According to Laplace-Young equation (Equation (1)), the pressure range of  $P_{\rm in}$  is due to the nanopore size distribution of SG90.

$$P_{in} = 2\gamma \cdot \cos\theta / r \tag{1}$$

where  $\gamma$  is the excessive solid-liquid interfacial tension,  $\theta$  is the contact angle and r is the nanopore radius. The width of the stress plateau,  $W_{\rm in}$ , determined by the total pore volume of SG90, is around 500 mm<sup>3</sup>/g.

Upon unloading, the stress drops abruptly, resulting in a highly hysteric behavior of the LN system.

As the concentration of ethanol increases to 10 wt%, the working pressure of LN-2 decreases to 8–20 MPa. As the ethanol concentration further increases to 15 wt%, the working pressure of LN-3 drops to 5–12 MPa. The decrease in working pressure of LNs is due to the reduced surface tension of the aqueous solution. When the ethanol concentration increases from 0 to 15 wt%, the surface tension of the aqueous solution,  $\gamma$ , decreases [57]. According to Equation (1), the infiltration pressure  $P_{\rm in}$  of the LN systems is reduced. While changing the liquid surface tension through ethanol concentration adjustment, the nanoporous particle as well as the porous structure (Fig. 2) remain the same. Consequently, the total nanopore volume available for liquid infiltration is kept as a constant, leading to the same compressibility of the three different LN systems. Table 1 summarizes the material properties of LNs used in this

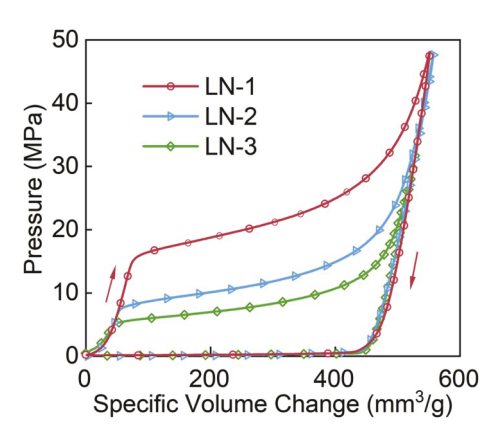


Fig. 5. Typical liquid infiltration behavior of LNs.

study. As shown in Table 1, LN fillers with different working pressure and same compressibility are achieved.

#### 3.3. Quasi-static compressive behavior of LNFTs

Fig. 6a shows typical compressive behavior of LNFTs containing different LN fillers. As the tube is filled with LN, the buckling initiation stress remains the same as that in empty tube. After buckling initiation, the stress drops due to the air bubbles trapped in between the nanoporous particles, i.e. the initial mechanical response is similar to the empty tube due to this small amount of air. At strain of 0.2, the internal pressure builds up and the LN filler starts to take effect. For the LN-1 filled tube, the stress quickly rises to 20 MPa and the system becomes highly compressible. A stress plateau with mean buckling stress of 20 MPa can be observed. This plateau matches well with the liquid infiltration behavior of the LN fillers, which reflects that the liquid infiltration has been triggered during buckling due to the confinement effect of the tube wall. The width of the plateau, W, is 20% of the effective height of the LN tube. As the strain reaches 0.4, the tube cracks, which leads to the leakage of the LN filler. From this point, the LNFT deforms like empty tube with vertical crack and shows reduced post-buckling strength compared to empty tube [52]. As shown in Fig. 6b, the LNFT buckles at two sites along the tube length, forming two visible wrinkles. As the buckling progresses, only one of them keeps growing until burst occurs, which is consistent with literature [34]. The buckling of the LNFT is in a concertina mode with asymmetrical outward wrinkles [58].

As the filler changes from LN-1 to LN-2, the initial stress of the enhanced post-buckling stress plateau,  $\sigma_0$ , decreases from 20 MPa to 14 MPa, which is attributed to the different initial working pressure  $P_i$  of these two LN-fillers. Similarly, as the filler changes to LN-3,  $\sigma_0$  is further reduced to 12 MPa. However, the plateau width increases to 30% of the initial tube height. The extended plateau is due to the increased amount of nanopores involved in liquid infiltration before the tube reaches its burst stress. According to classic theory, the thin-wall tube cracks as the hoop stress reaches its fracture strength. Thus,

$$P = \frac{2 \cdot \sigma_t \cdot t}{D} \tag{2}$$

where *P* is maximum internal pressure, and  $\sigma_t$  is the fracture stress of the

**Table 1**The material properties of LNs.

	Nanoporous	Liquid	$P_{\rm in}$ (MPa)		$W_{\rm in}~({\rm mm}^3/{\rm g})$
	Particles	Phase	$P_{\rm i}$	$P_{ m f}$	
LN-1	SG90	water	15	35	500
LN-2	SG90	10 wt% ethanol solution	8	20	500
LN-3	SG90	15 wt% ethanol solution	5	12	500

tube wall material. When  $P_f > P$ , only part of the nanopores are activated for liquid infiltration before tube bursts. As  $P_f$  decreases, more nanopores are involved, and thus the compressibility of the LN and the LNFT are enhanced. Accordingly, it is essential to match  $P_f$  and  $\sigma_t$  to optimize the energy mitigation performance of the resulted LNFTs. Moreover, increase of the LN filler compressibility,  $W_{\rm in}$ , leads to a prolonged filler-tube wall interaction, and thus more energy mitigation capacity.

The results of quasi-static compression tests are summarized in Table 2. The energy mitigation capacity is calculated by

$$E = \int F \, d\delta \tag{3}$$

The energy mitigation capacity of the empty tube at a total strain of 0.5 is 1843 J. For LNFTs, the LN-3 filled tube exhibits the best performance due to an optimized combination of  $P_{\rm i}$  and W. Only LN-3 filled tube is further analyzed in the following discussion. The energy mitigation capacity of LN-3 filled tube is 2678 J, which shows a 45% increase compared with empty tube. The increase of energy mitigation capacity is due to the extended compressibility of LN as well as the liquid-solid interaction between the LN and tube wall.

#### 3.4. Dynamic behavior of LNFTs

Fig. 7 represents typical dynamic stress-strain curves of LNFTs. Only LN-3 filled tube is evaluated here in dynamic tests, since it has the best quasi-static performance. Under gas gun impact, the initial buckling stress is lower than that of quasi-static test since LN is not triggered yet. The LN takes effect at about a strain of 0.18, after which the stress level increases dramatically. The average post-buckling strength of the LNFT under gas gun impact is 19.3 MPa, 36% higher than that in the quasistatic compression test, i.e. the crush performance of LNFT is strain rate sensitive. Please note that the maximum stress response of the LNFT under dynamic impact is similar to the value under quasi-static loading condition. At 0.6 strain, the stress quickly drops to 0 without any tube wall failure. The extremely high incident energy has been completely mitigated by the LNFT, which is not expected. The kinetic energy carried by the carriage is designed to be 1.5 times of the energy mitigation capacity of the LNFT under quasi-static loading condition. Fig. 8 shows the snapshots of the LNFT under gas gun impact. Similar to that in quasistatic compression, one visible fold is firstly formed at the top of the specimen. As the buckling progresses, another dominating fold is developed and buckles outwards in a concertina mode. With increased sample deformation, the second fold continuously expands and the cross-sectional area of the LNFT increases.

The results of energy mitigation capacity of LNFTs are summarized in Table 3. The *E* of LNFT under gas gun impact is 4130 J, which is increased by 54% compared with that in quasi-static compression. The strain rate sensitivity of LNFT agrees well with our previous result in Ref. [52], indicating that LN-filled structure has better energy mitigation performance under highly dynamic conditions.

## 3.5. Effect of tube wall material

Despite of the energy mitigation improvement of LNFTs, the total mass of LNFT increases and the specific energy absorption capacity (SEA) is only 14.0 J/g, showing negligible improvement compared with the SEA of empty tubes (13.9 J/g).

$$SEA = \frac{\int F \, d\delta}{m} \tag{4}$$

This is inconsistent with our previous results. In Ref. [52], the SEA of LNFT shows an increase of 55% compared with that of empty tube. The width of the enhanced post-buckling stress plateau is 60% of the initial tube height and the tube burst stress is much higher than the tube buckling initiation stress. While in current work the width is 40% of

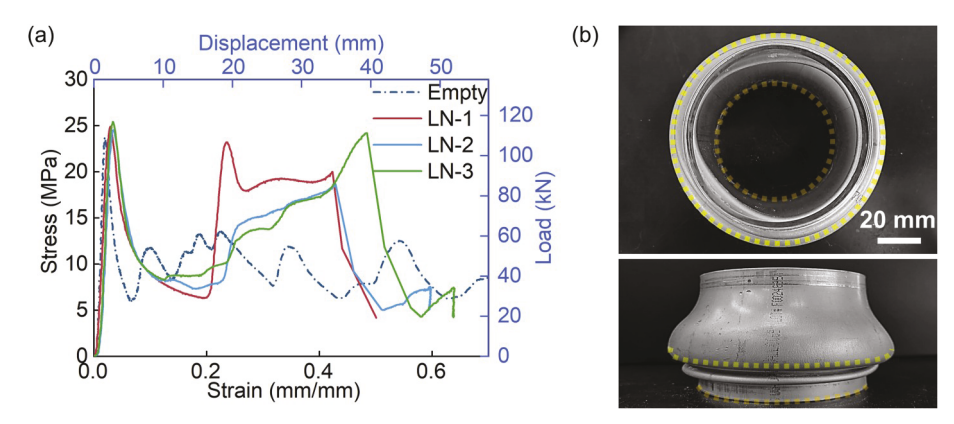
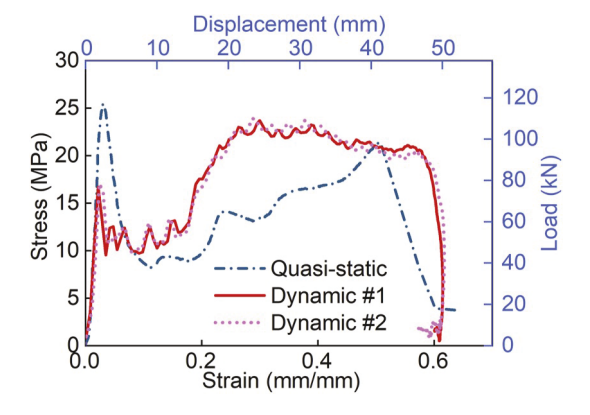


Fig. 6. (a) Typical stress-strain curves of LNFTs under quasi-static compression. Stress-strain and load-displacement axes are interchangeable. (b) Snapshots of the deformation mode of LNFTs under quasi-static compression. The yellow lines denote the lobe shape. (For interpretation of the references to color in this figure legend, the reader is referred to the Web version of this article.)

Table 2
Comparison of empty, and LN-filled tubes under quasi-static compression tests.

	1 0 -		-		•	
$\epsilon = 0$ –0.5	Sample Number	Mass (g)	P <sub>i</sub> (MPa)	$\sigma_0$ (MPa)	W	E (J)
Empty Tube  LNFT LN-1 LN-2 LN-3	#1 #2 #1 #1 #1 #2	134 132 313 302 297 294	N/A N/A 15 8 5	N/A N/A 20 14 12	N/A N/A 20% 20% 30% 30%	1843 1825 2281 2562 2663 2678



**Fig. 7.** Typical stress-strain curves of LNFTs under quasi-static compression and gas gun impact. Stress-strain and load-displacement axes are interchangeable.

initial tube height and the burst stress is lower than buckling initiation stress. These "contradictive" results are attributed to the different tube wall materials, Al in current work and stainless steel in previous work. As previously discussed, the post-buckling stress plateau is due to the liquid infiltration and the plastic deformation caused by the enhanced LN-tube wall interaction. According to Ref. [52], the foam strengthening coefficient is 3.8 for LNFT, much higher than conventional solid foam-filled tube. That is, the filler-tube interaction is much enhanced in LNFT and more severe plastic deformation of the tube wall is generated, which will be further validated in the following section. Therefore, once the strength limit of the tube material is reached upon this plastic deformation, the tube cracks, terminating the stress plateau immediately. Thus, the performance of LNFT is sensitive to the tube material.

To demonstrate this, quasi-static tensile test (standard ISO 6892-1:2019 [59]) is conducted on the tube which is pre-cut into rectangular shape by an Instron universal tester (Model 5982, Instron, Inc.).

Fig. 9 shows typical tensile behavior of both tube wall materials. The results of the material properties are summarized in Table 4. These results have demonstrated that the tube wall material affects the performance of LNFT in two folds. Firstly, the stiffness significantly affects the starting point of the enhanced post-buckling stress plateau in LNFT. The stiffness of Al is much lower than that of stainless steel. Therefore, more deformation is required to reach the yielding strength of the tube material. This has been validated by the strain at which the post-buckling stress plateau starts. For stainless steel tube the strain value is 0.1, while for Al tube the value is doubled. Secondly, the elongation at break determines the ending point of the stress plateau of LNFT. For stainless steel, the elongation at break is 65%, much higher than that of Al (only 17%). As a result, the plateau width of LN-filled stainless steel tube is much larger than that of LN filled Al tube. Therefore, to achieve optimized performance, stiff and ductile tube wall material to endure the much-enhanced filler-tube interaction is desired.

## 3.6. Energy absorption efficiency

The energy absorption efficiency ( $\eta$ ) [16,60], also known as crush force efficiency [25,61] or undulation of load carrying capacity [62], is often adopted to evaluate the uniformity and stability of the crush force of an energy absorber.  $\eta$  is defined as the ratio of the actual absorbed energy to the ideal absorbed energy over the same range of strain:

$$\eta = \frac{\int \sigma \, d\varepsilon}{\sigma - \varepsilon} \tag{5}$$

where  $\sigma_{\rm max}$  is the maximum stress over the calculated strain range. Higher value of  $\eta$  indicates that the energy absorber has a more stable force response as well as a better crashworthiness performance.

Fig. 10 shows the energy absorption efficiency  $\eta$  of the empty tubes and LNFTs for different strain ranges under both quasi-static and gas gun impact. Under gas gun impact, the  $\eta$  of empty tubes gradually increases to a maximum value 0.52 and then slowly drops with the increasing strain. The trend correlates well with the fluctuations of the stress-strain curves in Fig. 4a. For LNFTs, the  $\eta$  keeps increasing from 0.6 to 0.77 with the progressive buckling. Thus, LNFTs show a much higher energy absorption efficiency compared to empty tubes, due to the smaller stress fluctuations of LNFTs in Fig. 7.

#### 3.7. LN-tube wall interaction

The LN-tube wall interaction under quasi-static condition is quantified by the strengthening coefficient C as [33].

$$\sigma_{0ft} = \sigma_{0e} + C \,\sigma_{0f} \tag{6}$$

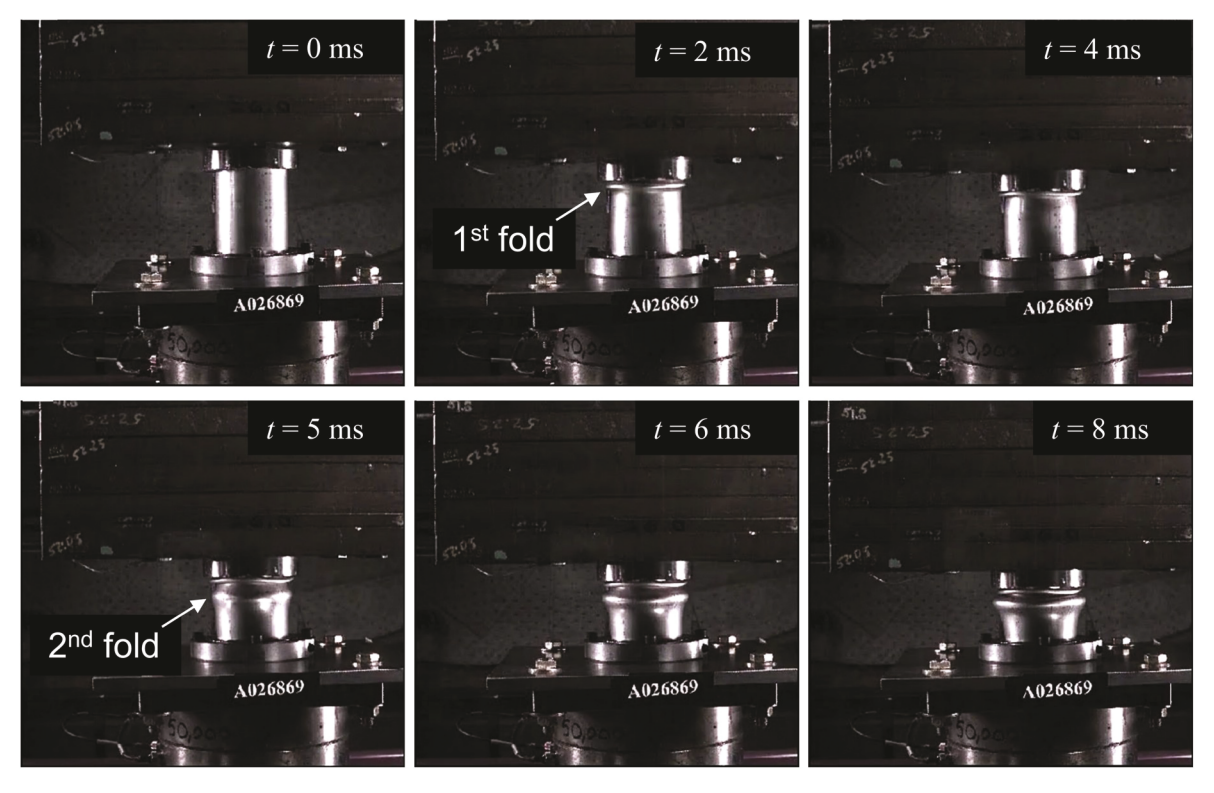


Fig. 8. Snapshots of the deformation mode of LNFTs under gas gun impact.

Table 3
Comparison of LNFTs under quasi-static compression and gas gun impact.

	Sample Number	Strain at burst	Average post-buckling strength, (MPa)	<i>E</i> (J)
Quasi-Static	#1	0.5	14.8	2663
	#2	0.5	14.9	2678
Gas Gun	#1	N/A	19.3	4117
Impact	#2	N/A	19.3	4130

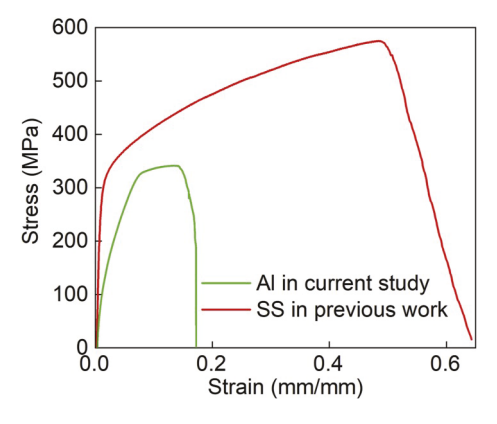


Fig. 9. Typical stress-strain curves of the tube wall materials Al and stainless steel under tensile test.

where,  $\sigma_{0f}$ ,  $\sigma_{0e}$  and  $\sigma_{0f}$  are the average post-buckling strength for the composite tube, empty tube and filler, respectively. Since the tube and the LN-filler have same nominal cross-sectional area and height,

$$E_{LNFT}^{Q} = E_e^{Q} + C E_{LN}^{Q} \tag{7}$$

where,  $E_{LNFT}^Q$ ,  $E_e^Q$  and  $E_{LN}^Q$  are the energy mitigation capacity of LNFT,

**Table 4**The mechanical properties of the tube wall materials, Al and stainless steel.

	Young's modulus (GPa)	Elongation at break (%)	Average stress after yielding (MPa)
Al	60	17	325
Stainless steel	215	65	500

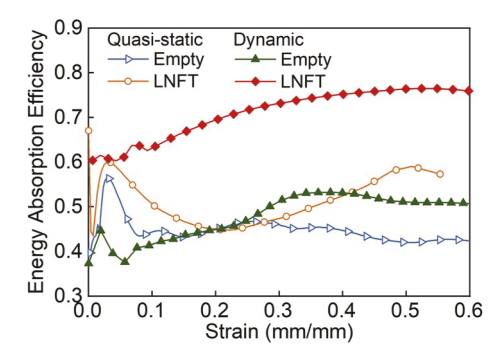
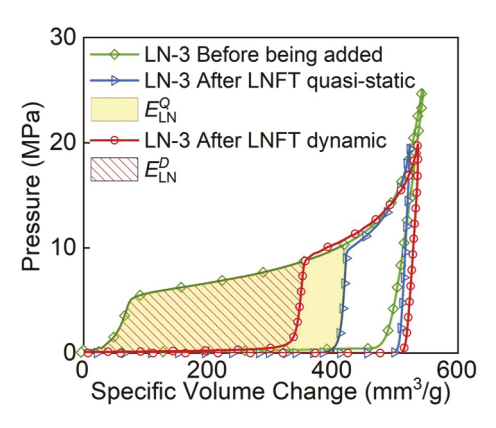


Fig. 10. The energy absorption efficiency of empty tubes and LNFTs under quasi-static compression and gas gun impact.

empty tube and LN-filler under quasi-static conditions, respectively. As strain increases,  $E_{LNFT}^Q$  and  $E_e^Q$  can be calculated from enclosed area by the curves in Fig. 6a. Due to the tube burst, not all the nanoporous materials are involved in liquid infiltration, as shown in Fig. 11. After the completion of quasi-static compression or dynamic impact tests, the LN-3 fillers have shown reduced liquid infiltration behavior, which depends on the loading condition. Accordingly, the total  $E_{LN}^Q$  is determined by the consumed energy mitigation capacity of LN-3 during the quasi-static compression (shaded area in Fig. 11). The corresponding  $E_{LN}^Q$  at different strains is calculated by assuming the consumption of LN is



**Fig. 11.** Typical liquid infiltration behavior of LN-3 filler after the completion of quasi-static compression or dynamic impact testing on LNFTs.

linearly proportional to the strain.

The LN-tube wall interaction under dynamic condition is quantified by the nominal strengthening coefficient  $C_n$  in a similar manner as

$$E_{LNFT}^D = E_e^D + C_n E_{LN}^D \tag{8}$$

where,  $E_{LNFT}^{D}$  and  $E_{e}^{D}$  are the energy mitigation capacity of LNFT and empty tube under dynamic conditions, respectively.  $E_{LN}^{D}$  is determined by the consumed energy mitigation capacity of LN-3 under dynamic impact (hatched area in Fig. 11).

Fig. 12 shows the results of the quasi-static strengthening coefficient, C, and the dynamic nominal strengthening coefficient,  $C_n$ , as the tube buckling progresses. The average C of the LNFT is around 3.5, which is consistent with our previous results of small-scale LNFT [52]. The average  $C_n$  of the LNFT is about 8.0. The large strengthening coefficients under both quasi-static and dynamic conditions indicate that stronger filler-tube wall interaction, which is attributed to the maintained intimate contact between LN and tube wall due to the fluidity and liquid infiltration behavior of the LN-filler.

The LN contributes to improve the filler-tube wall interaction by two main mechanisms: (i) load transfer effect from the tube wall to the LN and (ii) suppression of inward buckling. The enhanced contact area between LN filler and tube wall significantly improves the load transfer at the interface and prevents load drop due to tube wall collapse (Figs. 6a and 7). The suppression of the inwards buckling (Fig. 6b) increases the effective cross-sectional area of the composite tube. More importantly, the extent of plastic deformation of the tube wall is remarkably promoted, resulting in higher strain hardening of the metallic tube wall [63,64]. That is, the outwards buckling triggers the potential energy mitigation capacity of the tube wall material.

The enhanced plastic deformation of the tube wall due to LN-tube

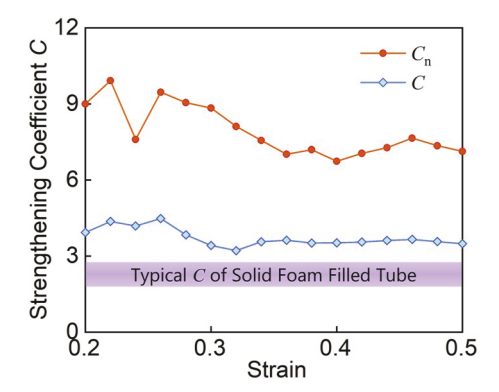


Fig. 12. Strengthening coefficient C at different strains under quasi-static compression test and dynamic impact test.

wall interaction is further quantified by micro-CT imaging. The tube wall profiles of empty tube and LNFT after tests are captured by a micro-CT scanning system (Model QuantumGX, PerkinElmer Inc.) and the wall thickness along the profiles is measured, as shown in Fig. 13a. The original wall thickness is 1.63 mm as indicated by the white color. The wall thickness of empty tube increases at folds with a maximum value of about 2 mm and decreases to about 1.60 mm between adjacent folds. The thickness changes imply that the tube undergoes a combination of two deformation modes: severe compression at folds and slight tension between folds. The extent of thickness changes indicates that the compression at folds is dominant, while the majority of tube wall, i.e. tube wall between adjacent folds, shows little deformation. As the tube is filled with LN, the first fold (lower one) is similar to that in empty tube due to the small amount of air trapped in LN. As the LN starts to take effect, the second fold (upper one) is formed. The wall thickness of LNFT decreases to a minimum value of 1.41 mm. Therefore, the tube wall deformation is dominated in tension. Fig. 13b shows the thickness change of empty tube and LNFT. It can be observed that 60% of the empty tube wall deforms mainly in compression, while over 90% of the LNFT wall is heavily stretched. The column area represents the level of plastic deformation in the tube. Thus, the total plastic deformation has been increased by more than three times due to the addition of the LNfiller to the empty tube.

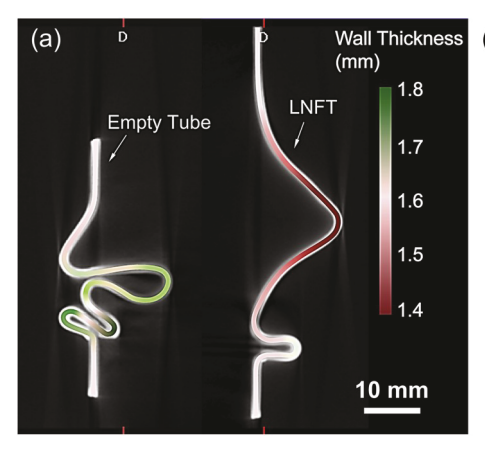
## 3.8. Effect of incident speed

The LNFTs show strong strain rate dependency (Fig. 7), while the strain rate dependency of empty tube is negligible (Fig. 4a). The strain rate dependency is also reflected by the strengthening coefficients. As shown in Fig. 12, when the loading speed increases from 2 mm/s to 6.7 m/s, the strengthening coefficient increases from C = 3.5 to  $C_n = 8.0$ . In our previous small-scale LNFT study [52],  $C_n = 4.2$  with an incident speed of 3.0 m/s. The strain rate dependency is nonlinear and tends to converge at high strain rates. The ratio of the filler-tube wall interfacial area to filler volume is proportional to 1/D. Therefore, the normalized filler-tube wall interface for unit volume of LN-filler in the current large-scale LNFT is only 1/6 of the small-scale one. As the filler-tube wall interaction is proportional to the interfacial area, the enhanced  $C_n$  of the large-scale LNFT cannot be explained by the much smaller normalized interfacial area.

Possibly, the energy mitigation capacity of the LN-filler is increased at high strain rates due to the non-dissipative nanofluidic energy capture mechanism [45-47]. This enhanced energy mitigation performance of the LN-filler contributes to the increased  $C_n$ , in addition to the LN-tube wall interaction at high strain rates. Upon impact the liquid molecules are forced into the nanopores at  $P_{\rm in}$ . Different from the quasi-static compression case, the liquid molecules carry not only potential energy but also high kinetic energy into the nanopores. Due to the mechanical impedance mismatch between the trapped liquid molecules and the rigid nanopore wall, the energy transportation path is severely distorted by the 3D nanoporous network. Thus, the incident energy of the external impact is redirected and captured in the nanopores. The energy capture capacity increases dramatically with the incident speed. Xu et al. [45] has demonstrated that the captured energy at incident speed of 30 m/s is 8 times that in quasi-static conditions via MD simulation. Lu [46] has reported enhanced energy dissipation of LN at 15 m/s in Split Hopkinson Pressure Bar testing condition. This enhanced energy mitigation capability of LN together with the strong LN-tube wall interaction and extended tube wall tension, make the resulted LNFTs promising for advanced energy absorber with extremely high energy mitigation capacity and adaptive to strain rate and input energy level.

#### 4. Conclusion

In this study, the crush performance of large-scale LNFTs at different strain rates, i.e. quasi-static compression and gas gun impact testing



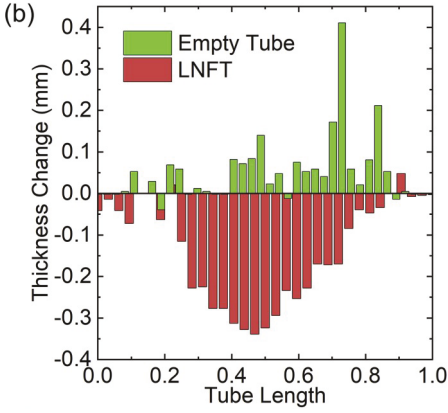


Fig. 13. (a) micro-CT images of empty tube and LNFT (b) Thickness change of empty tube and LNFT along the tube length.

conditions, has been experimentally evaluated. The performance of LNFTs in current study has been compared to that of empty tube as well as the small-scale LNFTs in our previous work. In conclusion:

- (1) The LN filler significantly promotes the post-buckling strength from 10.8 MPa (empty tube) to 19.3 MPa (LNFT) under dynamic impact. This 79% increase is due to the high energy absorption capacity of LN filler and the enhanced LN-tube wall interaction.
- (2) The LN-tube interaction improves the energy mitigation performance of LNFTs by promoting the plastic deformation of the tube wall. As demonstrated by micro-CT, the plastic deformation of the tube wall in LNFT is enhanced by more than three times, which engages more tube material to participate in the energy mitigation and improves the crushing resistance of the whole structure.
- (3) The LN-tube wall interaction at high strain rates is significantly enhanced with a strengthening coefficient of 8.0 and much stronger than that in solid foam-filled tube due to the maintained intimate contact between the fluid-like LN-filler and the tube wall.
- (4) The energy mitigation capacity of the LNFTs under dynamic impact shows 54% increase compared to that under quasi-static compression. This is due to the non-dissipative nanofluidic energy capture mechanism of the LN filler. The high strain rate sensitivity of LNFT makes it a promising adaptive energy mitigation structure under dynamic loading conditions.
- (5) The LNFT exhibits an energy absorption efficiency of 0.77, 48% higher than the value of empty tubes, 0.52. The high energy absorption efficiency of LNFT is due its relatively stable crush force response.
- (6) The working pressure of LN filler determines the post-buckling stress level of LNFT. To optimize the energy mitigation capacity of LNFT, the working pressure of LN should match the tube fracture strength.
- (7) The mechanical properties of tube wall material are of great importance in the design of LNFT. To achieve optimized performance, stiff and ductile tube wall material to endure the muchenhanced filler-tube interaction is desired.

#### Declaration of competing interest

The authors declare that they have no known competing financial interests or personal relationships that could have appeared to influence the work reported in this paper.

## CRediT authorship contribution statement

Mingzhe Li: Methodology, Investigation, Data curation, Formal

analysis, Writing - original draft. Saeed Barbat: Writing - review & editing, Project administration. Ridha Baccouche: Writing - review & editing, Project administration. Jamel Belwafa: Investigation, Writing - review & editing. Weiyi Lu: Conceptualization, Data curation, Writing - review & editing, Supervision, Funding acquisition, Project administration.

## Acknowledgement

The authors would like to thank Mr. Jeremy Hix and Dr. Erik Shapiro for the help on micro-CT imaging capture. The characterization of LNFTs are supported by Ford-MSU Alliance program and the data analysis is supported by the National Science Foundation (NSF) (No. CBET-1803695).

#### References

- [1] Lu G, Yu TX. Energy absorption of structures and materials. CRC Press; 2003.
- [2] Wierzbicki T, Abramowicz W. On the crushing mechanics of thin-walled structures. J Appl Mech 1983;50:727–34.
- [3] Chen W, Wierzbicki T. Relative merits of single-cell, multi-cell and foam-filled thin-walled structures in energy absorption. Thin-Walled Struct 2001;39:287–306.
- [4] Fang J, Sun G, Qiu N, Kim NH, Li Q. On design optimization for structural crashworthiness and its state of the art. Struct Multidiscip Optim 2017;55: 1001–110.
- [5] Baroutaji A, Sajjia M, Olabi A-G. On the crashworthiness performance of thinwalled energy absorbers: recent advances and future developments. Thin-Walled Struct 2017;118:137–63.
- [6] Duarte I, Krstulović-Opara L, Vesenjak M. Axial crush behaviour of the aluminium alloy in-situ foam filled tubes with very low wall thickness. Compos Struct 2018; 192-184-92.
- [7] Su M, Wang H, Hao H. Axial and radial compressive properties of aluminaaluminum matrix syntactic foam filled thin-walled tubes. Compos Struct 2019;226: 111197.
- [8] Duarte I, Krstulović-Opara L, Vesenjak M. Characterisation of aluminium alloy tubes filled with aluminium alloy integral-skin foam under axial compressive loads. Compos Struct 2015;121:154–62.
- [9] Hangai Y, Saito M, Utsunomiya T, Kitahara S, Kuwazuru O, Yoshikawa N. Fabrication of aluminum foam-filled thin-wall steel tube by friction welding and its compression properties. Materials (Basel) 2014;6:6796–810.
- [10] Pan L, Yang Y, Ahsan MU, Luong DD, Gupta N, Kumar A, et al. Zn-matrix syntactic foams: effect of heat treatment on microstructure and compressive properties. Mater Sci Eng A 2018;731:413–22.
- [11] Costas M, Morin D, Langseth M, Romera L, Díaz J. Axial crushing of aluminum extrusions filled with PET foam and GFRP. An experimental investigation. Thin-Walled Struct 2016;99:45–57.
- [12] Liu Q, Fu J, Wang J, Ma J, Chen H, Li Q, et al. Axial and lateral crushing responses of aluminum honeycombs filled with EPP foam. Compos B Eng 2017;130:236–47.
- [13] Movahedi N, Murch GE, Belova IV, Fiedler T. Manufacturing and compressive properties of tube-filled metal syntactic foams. J Alloys Compd 2020;822:153465.
- [14] Linul E, Lell D, Movahedi N, Codrean C, Fiedler T. Compressive properties of zinc syntactic foams at elevated temperatures. Compos B Eng 2019;167:122–34.
- [15] Myers K, Katona B, Cortes P, Orbulov IN. Quasi-static and high strain rate response of aluminum matrix syntactic foams under compression. Compos Appl Sci Manuf 2015;79:82–91.

- [16] Wang H, Su M, Hao H. The quasi-static axial compressive properties and energy absorption behavior of ex-situ ordered aluminum cellular structure filled tubes. Compos Struct 2020;239:112039.
- [17] Fang J, Gao Y, An X, Sun G, Chen J, Li Q. Design of transversely-graded foam and wall thickness structures for crashworthiness criteria. Compos B Eng 2016;92: 338–49.
- [18] Yi Z, Si-yuan H, Jia-gui L, Wei Z, Xiao-lu G, Jin Y. Density gradient tailoring of aluminum foam-filled tube. Compos Struct 2019;220:451–9.
- [19] Movahedi N, Murch GE, Belova IV, Fiedler T. Functionally graded metal syntactic foam: fabrication and mechanical properties. Mater Des 2019;168:107652.
- [20] Yin H, Dai J, Wen G, Tian W, Wu Q. Multi-objective optimization design of functionally graded foam-filled graded-thickness tube under lateral impact. Int J Comput Methods 2019;16:1850088.
- [21] Sun G, Liu T, Huang X, Zheng G, Li Q. Topological configuration analysis and design for foam filled multi-cell tubes. Eng Struct 2018;155:235–50.
- [22] Sun G, Wang Z, Yu H, Gong Z, Li Q. Experimental and numerical investigation into the crashworthiness of metal-foam-composite hybrid structures. Compos Struct 2019;209:535–47.
- [23] Zhang Y, Sun G, Li G, Luo Z, Li Q. Optimization of foam-filled bitubal structures for crashworthiness criteria. Mater Des 2012;38:99–109.
- [24] Zhou J, Guan Z, Cantwell WJ. The energy-absorbing behaviour of composite tubereinforced foams. Compos B Eng 2018;139:227–37.
- [25] Zhu G, Liao J, Sun G, Li Q. Comparative study on metal/CFRP hybrid structures under static and dynamic loading. Int J Impact Eng 2020:103509.
- [26] Zhang Z, Sun W, Zhao Y, Hou S. Crashworthiness of different composite tubes by experiments and simulations. Compos B Eng 2018;143:86–95.
- [27] Yin H, Liu Z, Dai J, Wen G, Zhang C. Crushing behavior and optimization of sheet-based 3D periodic cellular structures. Compos B Eng 2020;182:107565.
- [28] Lu C, Hou S, Zhang Z, Chen J, Li Q, Han X. The mystery of coconut overturns the crashworthiness design of composite materials. Int J Mech Sci 2020;168:105244.
- [29] Hanssen AG, Langseth M, Hopperstad OS. Static crushing of square aluminium extrusions with aluminium foam filler. Int J Mech Sci 1999;41:967–93.
- [30] Santosa S, Wierzbicki T. Crash behavior of box columns filled with aluminum honeycomb or foam. Comput Struct 1998;68:343–67.
- [31] Bonaccorsi L, Proverbio E, Raffaele N. Effect of the interface bonding on the mechanical response of aluminium foam reinforced steel tubes. J Mater Sci 2010; 45:1514–22.
- [32] Toksoy AK, Güden M. The strengthening effect of polystyrene foam filling in aluminum thin-walled cylindrical tubes. Thin-Walled Struct 2005;43:333–50.
- [33] Santosa SP, Wierzbicki T, Hanssen AG, Langseth M. Experimental and numerical studies of foam-filled sections. Int J Impact Eng 2000;24:509–34.
- [34] Duarte I, Vesenjak M, Krstulović-Opara L, Ren Z. Compressive performance evaluation of APM (Advanced Pore Morphology) foam filled tubes. Compos Struct 2015;134:409–20.
- [35] Strano M, Villa A, Mussi V. Design and manufacturing of anti-intrusion bars made of aluminium foam filled tubes. Int J Material Form 2013;6:153–64.
- [36] Taherishargh M, Vesenjak M, Belova IV, Krstulović-Opara L, Murch GE, Fiedler T. In situ manufacturing and mechanical properties of syntactic foam filled tubes. Mater Des 2016:99:356–68.
- [37] Zhang Z, Liu S, Tang Z. Crashworthiness investigation of kagome honeycomb sandwich cylindrical column under axial crushing loads. Thin-Walled Struct 2010; 48:9–18.
- [38] Baroutaji A, Sajjia M, Olabi AG. On the crashworthiness performance of thinwalled energy absorbers: recent advances and future developments. Thin-Walled Struct 2017;118:137–63.
- [39] Li M, Lu W. Liquid marble: a novel liquid nanofoam structure for energy absorption. AIP Adv 2017;7:055312.
- [40] Li M, Xu L, Lu W. Nanopore size effect on critical infiltration depth of liquid nanofoam as a reusable energy absorber. J Appl Phys 2019;125:044303.

- [41] Liu L, Lim H, Lu W, Qiao Y, Chen X. Mechanical-to-electric energy conversion by mechanically driven flow of electrolytes confined in nanochannels. APEX 2013;6: 015202
- [42] Lu W, Han A, Kim T, Chow BJ, Qiao Y. Endcapping treatment of inner surfaces of a hexagonal mesoporous silica. J Adhes Sci Technol 2012;26:2135–41.
- [43] Zhang Y, Li M, Gao Y, Xu B, Lu W. Compressing liquid nanofoam systems: liquid infiltration or nanopore deformation? Nanoscale 2018;10:18444–50.
- [44] Li M, Lu W. Adaptive liquid flow behavior in 3D nanopores. Phys Chem Chem Phys 2017;19:17167–72.
- [45] Xu B, Chen X, Lu W, Zhao C, Qiao Y. Non-dissipative energy capture of confined liquid in nanopores. Appl Phys Lett 2014;104:203107.
- [46] Lu W. Novel protection mechanism of blast and impact waves by using nanoporous materials. Dyn Behav Mater 2016;1:177–83. 1, Springer International Publishing.
- [47] Xu B, Qiao Y, Chen X. Mitigating impact/blast energy via a novel nanofluidic energy capture mechanism. J Mech Phys Solid 2014;62:194–208.
- [48] Dean M. Jaradi, Mohammad Omar Faruque, S. M. Iskander Farooq. Accelerator pedal for vehicle incorporating liquid nanofoam. U.S. Patent 10,214,104, 2017.
- [49] Chen X, Surani FB, Kong X, Punyamurtula VK, Qiao Y. Energy absorption performance of steel tubes enhanced by a nanoporous material functionalized liquid. Appl Phys Lett 2006;89:1–3.
- [50] Sun Y, Xu J, Zhao C, Li P, Li Y. Exploring a new candidate of energy absorber: thinwalled tube structures filled with nanoporous material functionalized liquid. IRCOBI Conf 2014;2014:578–86.
- [51] Sun Y, Li Y, Zhao C, Wang M, Lu W, Qiao Y. Crushing of circular steel tubes filled with nanoporous-materials-functionalized liquid. Int J Damage Mech 2016:1–12.
- [52] Li M, Li J, Barbat S, Baccouche R, Lu W. Enhanced filler-tube wall interaction in liquid nanofoam-filled thin-walled tubes. Compos Struct 2018;200:120–6.
- [53] Borman VD, Belogorlov AA, Grekhov AM, Tronin VN. Fluctuations of the number of neighboring pores and appearance of multiple nonergodic states of a nonwetting liquid confined in a disordered nanoporous medium. Phys Lett A 2014;378: 2888–93.
- [54] Hanssen AG, Langseth M, Hopperstad OS. Static and dynamic crushing of circular aluminium extrusions with aluminium foam filler. Int J Impact Eng 2000;24: 475–507.
- [55] Kavi H, Toksoy AK, Guden M. Predicting energy absorption in a foam-filled thinwalled aluminum tube based on experimentally determined strengthening coefficient. Mater Des 2006;27:263–9.
- [56] Tucker MT, Horstemeyer MF, Whittington WR, Solanki KN, Gullett PM. The effect of varying strain rates and stress states on the plasticity, damage, and fracture of aluminum alloys. Mech Mater 2010:42:895–907.
- [57] Vazquez G, Alvarez E, Navaza JM. Surface tension of alcohol water + water from 20 to 50 .degree.C. J Chem Eng Data 1995;40:611–4.
- [58] Andrews KRF, England GL, Ghani E. Classification of the axial collapse of cylindrical tubes under quasi-static loading. Int J Mech Sci 1983;25:687–96.
- [59] ISO 6892-1. Metallic materials tensile testing Part 1: method of test at room temperature. 2019.
- [60] Taherishargh M, Vesenjak M, Belova IV, Krstulović-Opara L, Murch GE, Fiedler T. In situ manufacturing and mechanical properties of syntactic foam filled tubes. Mater Des 2016;99:356–68.
- [61] Sun G, Yu H, Wang Z, Xiao Z, Li Q. Energy absorption mechanics and design optimization of CFRP/aluminium hybrid structures for transverse loading. Int J Mech Sci 2019;150:767–83.
- [62] Ha NS, Lu G, Xiang X. High energy absorption efficiency of thin-walled conical corrugation tubes mimicking coconut tree configuration. Int J Mech Sci 2018;148: 409-21
- [63] Liu Y, Schaedler TA, Jacobsen AJ, Lu W, Qiao Y, Chen X. Quasi-static crush behavior of hollow microtruss filled with NMF liquid. Compos Struct 2014;115: 29–40.
- [64] Liu Y, Schaedler TA, Jacobsen AJ, Chen X. Quasi-static energy absorption of hollow microlattice structures. Compos B Eng 2014;67:39–49.